Journal of Inorganic and General Chemistry
ZAAC
Zeitschrift für anorganische und allgemeine Chemie
doi.org/10.1002/zaac.202100190
ARTICLE

Magnetic properties and structural analysis on spinel $MnFe_2O_4$ nanoparticles prepared *via* non-aqueous microwave synthesis

Christopher Simon,[a] André Blösser,[a] Mirco Eckardt,[a] Hannah Kurz,[a] Birgit Weber,[a] Mirijam Zobel[+],[a] and Roland Marschall*[a]

Dedicated to Prof. Dr. Josef Breu on the occasion of his 60th birthday

Phase-pure 6 nm spinel $MnFe_2O_4$ nanoparticles with high specific surface area of 145 $m^2 g^{-1}$ were successfully prepared *via* microwave-assisted non-aqueous sol-gel synthesis. The phase evolution during postsynthetic thermal treatment was investigated systematically by various methods, including powder X-ray diffraction (PXRD), pair distribution function (PDF) analysis, and Raman spectroscopy. Our results show that the material decomposes to non-spinel binary compounds α-Mn_2O_3 and α-Fe_2O_3 at temperatures between 400 and 600 °C. The application potential of $MnFe_2O_4$ nanoparticles with $3d^5$ Mn(II) and Fe(III) ions with respect to the magnetic properties was demonstrated by superconducting quantum interference device (SQUID) magnetometry, with the as-synthesized nanoparticles reaching a high saturation magnetization of 2.62 μ_B per formula unit (63.5 $Am^2 kg^{-1}$) at 10 K. We further highlight the visible-light response of synthesized powders, making the materials promising for light-related applications, *e.g.* photocatalytic hydrogen evolution. An important additional feature of $MnFe_2O_4$ nanoparticles is their good dispersibilty in polar or non-polar media, as a result of postsynthetic colloidal stabilization with betaine hydrochloride, oleic acid combined with oleylamine, or citric acid.

Introduction

In the last decades, preparation of inorganic magnetic nanoparticles (MNPs) has received particular attention due to their widespread application range, including biomedicine,[1] imaging,[2] data-storage,[3] spintronics,[4] or homogeneous and heterogeneous catalysis.[5–8] Among the variety of available magnetic nanomaterials, the spinel ferrite class offers a significant saturation magnetization, a high electrical resistance, low electrical losses, and an outstanding chemical stability.[9] In addition, most of these materials can be prepared from earth-abundant and inexpensive precursors.[10] Generally, the structure of spinel ferrites can be written as MFe_2O_4, where M represents divalent cations, *e.g.* Fe(II), Cd(II), Mg(II), Zn(II), Cu(II), Ni(II), Co(II), and Mn(II). The occupation of tetrahedral (A) and octahedral (B) sites in the ccp lattice depends on cationic sizes and crystal field splitting energies and is usually described by the inversion parameter λ, according to the notation $(M_{1-\lambda}Fe_\lambda)^A(M_\lambda Fe_{2-\lambda})^B O_4$. An inversion value of $\lambda = 0$ represents a normal spinel structure (*e.g.* $ZnFe_2O_4$),[11] $\lambda = 1$ points out an inverse spinel structure (*e.g.* $NiFe_2O_4$),[12] and the situation $0 < \lambda < 1$ is referred as partially inverse spinel.

Typically, antiferromagnetic exchange interactions result in a magnetic moment of both sublattices, which are coupled ferrimagnetically. The magnetic moment of a spinel ferrite can therefore be described as the difference of magnetic moments of A and B sublattices, with A–B interactions as the dominant ones, determining the overall antiferromagnetic or ferrimagnetic nature.[13,14] The interaction between B site cations are also antiferromagnetic, but much weaker.[15] Since the magnetism consequently depends on the cationic distributions, tailoring the inversion parameter provides a simple access to tune the magnetic properties of spinel ferrites. The degree of inversion can be modified by establishing non-equilibrium conditions, which can be achieved by preparing nanoparticulate materials. In other words, the particle size of a spinel ferrite directly influences λ, and therefore also the magnetism.[16–19]

Owning $3d^5$ electronic high-spin configuration of Mn(II) and Fe(III) centers,[20] manganese ferrite ($MnFe_2O_4$) is an interesting candidate for a functional material with a remarkable high saturation magnetization of 3.3–4.5 μ_B per formula unit for the bulk state.[21–23] The bulk saturation moment of $MnFe_2O_4$ is significantly higher than for other spinel ferrites, *e.g.* $NiFe_2O_4$ (2.2–2.3 μ_B),[24–26] or $MgFe_2O_4$ (1.1–1.4 μ_B),[17,27,28] and comparable to the ones of Fe_3O_4 (3.7–3.9 μ_B),[29–31] or $CoFe_2O_4$ (3.6–4.0 μ_B).[24,32,33] However, it should be noted that the influence of the inversion parameter on the magnetic properties is less pronounced for $MnFe_2O_4$, compared to other spinel ferrites,

[a] C. Simon, A. Blösser, M. Eckardt, H. Kurz, B. Weber, M. Zobel,[+] R. Marschall
Department of Chemistry, University of Bayreuth, Universitaetsstrasse 30, 95447 Bayreuth, Germany
E-mail: roland.marschall@uni-bayreuth.de
[+] Present address: Institute of Crystallography, RWTH Aachen University, 52066 Aachen, Germany

Supporting information for this article is available on the WWW under https://doi.org/10.1002/zaac.202100190

such as $MgFe_2O_4$ or Fe_3O_4. This is based on the fact that Mn(II) (A) and Fe(III) (B) cations exhibit an isoelectronic configuration ($3d^5$). But, theoretical DFT calculations by Huang *et al.* reveal saturation of 5 and 3 μ_B per formula unit for a normal and inverse spinel, respectively, which was confirmed by Simsa and Brabers experimentally.[15,34] This can be correlated to spin canting phenomena and/or mixed valence.[35,36] Spin canting describes the phenomenon that especially the spins of surface ions feature different orientations leading to altered magnetic moments. This effect is especially observed in nanostructures due to the finite-size effect. For the thermodynamically stable bulk state, degrees of inversion for $MnFe_2O_4$ of $\lambda = 0.15–0.2$ were reported, which are commonly estimated *via* neutron diffraction or Mössbauer spectroscopy. Therefore, $MnFe_2O_4$ crystallizes in a partially inverse spinel structure.[37,38] Non-equilibrium conditions can be established by preparing nanostructured spinel ferrites, with an often-altered degree of inversion. This was, for example, confirmed by Zhang *et al.* and Chen *et al.* for co-precipitated $MnFe_2O_4$ nanoparticles with sizes of < 10 nm respective 40 nm, with reported inversion degrees of $\lambda = 0.61–0.67$.[39,40] Thus, preparation of nanosized $MnFe_2O_4$ further allows fine-tuning of its magnetic properties. Moreover, featuring a band gap of 1.75–1.78 eV, $MnFe_2O_4$ is able to absorb large portion of sunlight and convert it into chemical energy.[41] For instance, pristine $MnFe_2O_4$ was already applied as photocatalyst for hydrogen evolution or degradation of methylene blue.[42–44] However, for liquid applications, *e.g.* as magnetic fluid[45] or heterogeneous (photo-)catalyst,[46] the colloidal stabilization of ferrimagnetic $MnFe_2O_4$ nanoparticles could be benefical, resulting in a better dispersibilty in aqueous or non-aqueous media. This would further reduce the risk of releasing harmful nanoparticle dusts into the air.[47] The ferrimagnetic nature of $MnFe_2O_4$ nanoparticles still enables a simple method for recovering. Common functionalization agents for the postsynthetic stabilization of Fe-based nanoparticles are oleic acid combined with oleylamine, betaine hydrochloride, or citric acid.[48–50]

$MnFe_2O_4$ nanoparticles with manifold morphological characteristics can be synthesized by different methods, including ball milling,[51] solvothermal synthesis,[52] hydrothermal synthesis,[53] and co-precipitation.[40,54] Compared to many traditional wet-chemical syntheses, the microwave synthesis as alternative offers high reproducibility, significantly shortened reaction times, efficient heating, and high yields.[55] In contrast to *e.g.* milling down solid-state synthesized materials to the desired particle size, microwave syntheses can yield relatively defect-free particles with function-tailored properties,[56] using a significantly lower energy input.

Following this, we present a fast and energy-saving microwave-assisted synthesis of 6 nm single-phase magnetic $MnFe_2O_4$ nanoparticles, which is based on the sol-gel reaction of the metal acetylacetonates with the high boiling point solvent *rac*-1-phenylethanol,[57,58] which was earlier applied to other spinel ferrite materials, such as $MgFe_2O_4$,[17,50] $ZnFe_2O_4$,[59] and $NiFe_2O_4$.[60] The thermal stability of the obtained $MnFe_2O_4$ nanoparticles was investigated by calcination at 400, 600, and 800 °C, showing that the material decomposes to binary non-spinel compounds α-Mn_2O_3 and α-Fe_2O_3 after calcination at 400 °C or higher. Special attention was paid on the magnetic properties of prepared materials, which can be correlated to both particle morphology and phase composition.

Results and discussion

Crystalline $MnFe_2O_4$ nanoparticles were synthesized *via* simple non-aqueous microwave-assisted synthesis. Therefore, the metal acetylacetonates dissolved in *rac*-1-phenylethanol (boiling point 204 °C) were treated at 250 °C for 30 minutes in a commercial microwave reactor (Figure S1), before precipitating the obtained particles with *n*-pentane. Afterwards, the particles were washed with acetone-water mixtures plus diethyl ether and dried at 80 °C. Subsequent thermal treatment in a muffle furnace at 400, 600, and 800 °C was additionally performed under air atmosphere to remove remaining organic residues completely and to investigate potentially occurring phase transformations.

The morphologies of obtained samples were investigated by Transmission Electron Microscopy (TEM) (Figures 1a–d). Selected Area Electron Diffraction (SAED) patterns of the obtained Mn–Fe–O samples are further presented in Figures 1e–h. Directly after synthesis, strongly agglomerated nanosized particles can be observed. The rings in the corresponding SAED pattern indicate a nanocrystalline nature of obtained particles and can be assigned to the spinel-type structure of *e.g.* manganese ferrite ($MnFe_2O_4$, JCPDS, no. 01-073-1964). However, the assignment to $MnFe_2O_4$ is not straightforward due to the breadth of observed rings. The nanoparticulate morphology, as well as the spinel-type crystal structure, are preserved when calcining the particles at 400 °C. Upon calcination at elevated temperatures (600 or 800 °C), the nanoparticulate morphology is lost. In the corresponding SAED patterns, diffraction spots are dominant instead of rings, which clearly confirm crystallite growth.

HR-TEM images of as-synthesized and 400 °C-treated samples presented in Figures 2a,c underline the high crystallinity of obtained nanoparticles. Lattice planes are visible even for the non-calcined nanoparticles. Associated particle size distributions (Figures 2b,d) were generated by counting of 100 nanoparticles. They can be fitted by a LogNormal function, giving similar particle mean diameters of 6.0 and 6.3 nm for as-synthesized and 400 °C-treated samples, respectively. Thus, no crystallite growth occurs when calcining the as-synthesized particles at 400 °C. The specific surface areas estimated *via* BET (*Brunauer-Emmett-Teller*) evaluation of N_2 physisorption data are 145 (as-synthesized) and 144 $m^2 g^{-1}$ (400 °C). As expected, specific surface areas decrease upon calcination to 21 (600 °C) and 5 $m^2 g^{-1}$ (800 °C) due to crystallite growth. Assuming sherical particles and a bulk density of 4.77 $g\,cm^{-3}$ for $MnFe_2O_4$,[61] theoretical particles sizes with such a surface area could be calculated to 8.7 nm for as-synthesized and 400 °C samples, respectively. Due to the high degree of agglomeration (*c.f.* Figures 1a,b), the real particles are smaller.

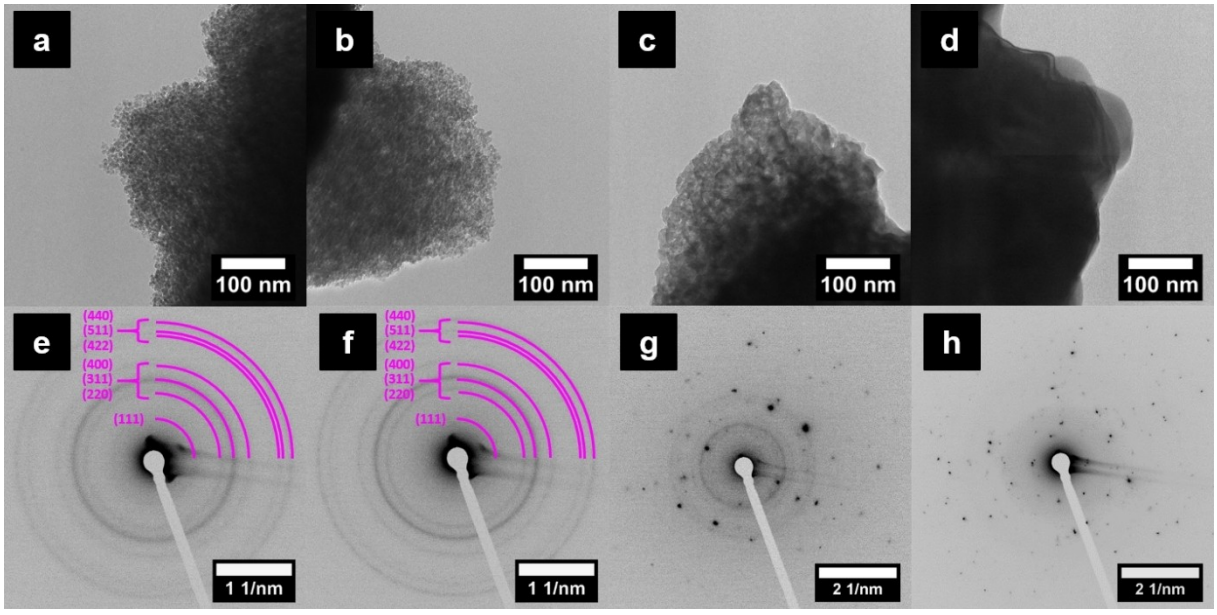

Figure 1. (a-d) Low-magnification TEM images of as-synthesized (left) and calcined (from mid-left to right: 400, 600, 800 °C) Mn–Fe–O samples. Corresponding SAED patterns are presented in (e–h).

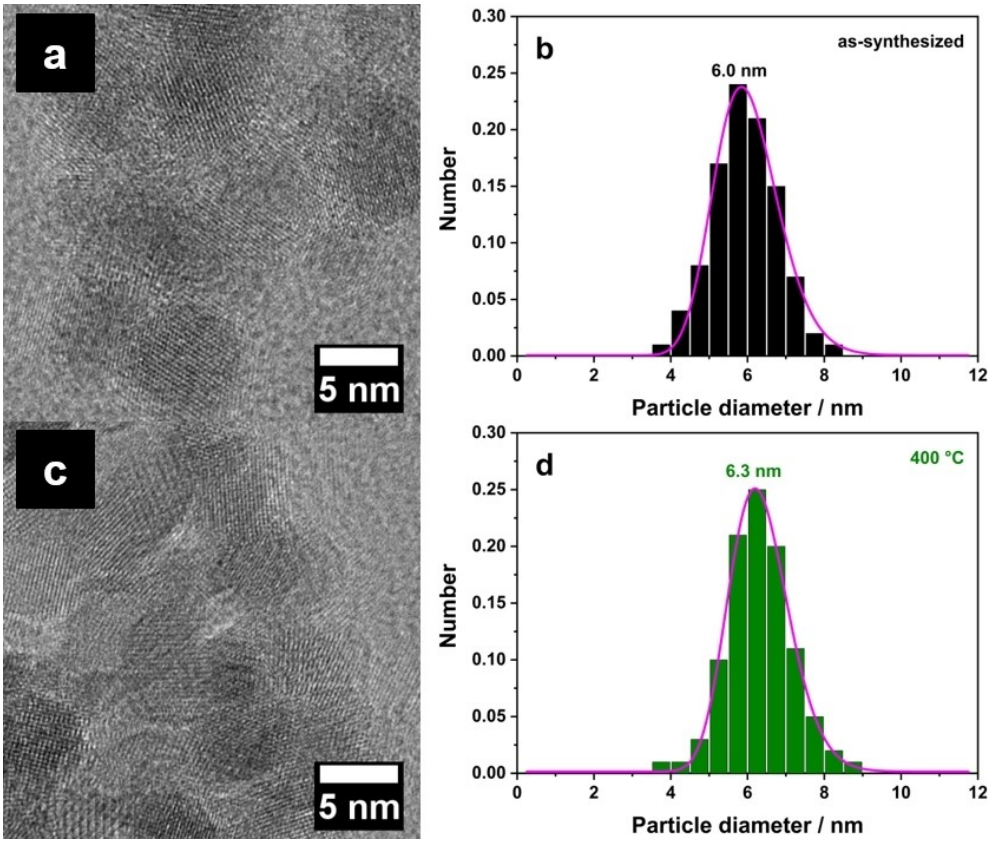

Figure 2. (a,c) HR-TEM images of as-synthesized and 400 °C-treated Mn–Fe–O nanoparticles and (b,d) associated particle size distributions fitted with a LogNormal function.

The phase composition of obtained Mn–Fe–O samples was investigated in detail by various techniques. PXRD patterns measured with silver (Figure 3) and copper (Figure S2) radiation reveal a cubic spinel structure for the as-synthesized and 400 °C-treated samples. Averaging integral breadth analysis of (220), (400), (511), and (440) reflections (Cu PXRD) yields crystallite sizes of 6.2 and 5.9 nm, respectively.[62] Therefore, particle and crystallite sizes are in the same range, which highlights the crystalline nature of prepared spinel nanoparticles.

The positions of the reflections for the as-synthesized nanoparticles are directly in between the ones of the calculated reference patterns for Fe_3O_4 and $MnFe_2O_4$. This could point towards domains of varying composition with Mn and Fe, a co-existence of phases, or an elemental gradient within the nanoparticles. Compared to the as-synthesized sample, the PXRD pattern of the 400 °C sample is shifted to higher *Q*-values, accompanied by the presence of an amorphous signal between 1.5 and 5.5 $Å^{-1}$ (Figure S3). This peak shift matches the modified lattice parameter as determined in PDF refinements. Finally, the sample has transitioned at 600 and 800 °C into co-existing α-Fe_2O_3 (hematite) and α-Mn_2O_3, with some residual spinel phase in the 600 °C sample. This strengthens the point that a phase separation sets in already at 400 °C into presumably an iron-rich spinel phase and nanoscale amorphous domains of manganese oxide.

In contrast to PXRD, which analyses crystal structures in reciprocal space based on Bragg reflections, the pair distribution function (PDF, Figure 4, Figures S4–S5) is gained *via* Fourier Transformation of PXRD data (including both diffuse and Bragg scattering) to real space. The PDF corresponds to a histogram of all interatomic distances in the sample, and is particularly useful when it comes to characterizing short-range order in disordered or nanomaterials. As suggested by PXRD, PDF refinements of the as-synthesized and the 400 °C sample reveal a spinel phase for both samples and a decrease of the lattice parameter caused by calcination. The best fit for the as-synthesized sample is based on two spinel structures, which differ in lattice parameters (and the scale). Since Mn(II) and Fe(III) have isoelectronic configuration, no distinction can be made between Fe_3O_4 and $MnFe_2O_4$ by neither PXRD nor PDF analysis. The stoichiometric ratio of Mn:Fe = 1:2 in $MnFe_2O_4$ was confirmed by energy-dispersive X-ray spectroscopy (EDXS, Figures S6a,c,e,g) and X-ray photoelectron spectroscopy (XPS, Figures S6b,d,f,h) analyses, giving averaged values of 0.51 and 0.47, respectively (EDXS: $Mn_{1.01}Fe_{1.99}O_4$, XPS: $Mn_{0.96}Fe_{2.04}O_4$). This underpins the likeliness of having a compositional or structural gradient in the as-synthesized sample with varying lattice parameters between 8.440 to 8.503 Å. Such gradients could be reflected, for instance, by either a core-shell model with varying lattice parameters from particle surface to core or the co-existence of Fe-rich ($Mn_{1-y}Fe_{2+y}O_4$) and Fe-poor ($Mn_{1+y}Fe_{2-y}O_4$) domains. A defect structure like γ-Fe_2O_3 can be excluded, as the occupancy of the octahedral sites is close to 1, as shown before in PDF refinements on spinel ferrite and iron oxide nanoparticles.[63,64]

While from PXRD data, we could only speculate about the existence of an amorphous Mn_2O_3 phase in the higher background of the 400 °C sample, PDF analysis explicitly confirms the formation of small 0.62 nm α-Mn_2O_3 domains. The addition of a α-Mn_2O_3 phase to the refinement with the spinel phase clearly improves the refinement from a goodness-of-fit R_w of 0.18 to 0.15. This proves that at 400 °C, the spinel phase with a certain distribution of lattice parameters has already started to transform into a spinel phase of shortened lattice parameters

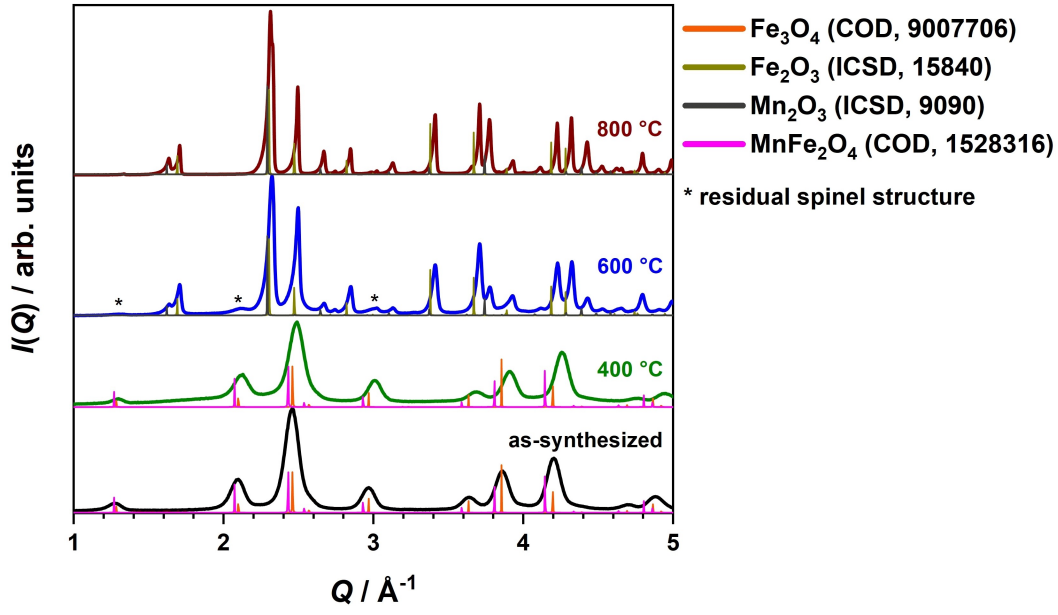

Figure 3. PXRD pattern of samples directly after synthesis and after calcination at 400, 600, and 800 °C. The patterns are stacked and scaled for clarity. Calculated reference patterns of Fe_3O_4, $MnFe_2O_4$, α-Fe_2O_3, and α-Mn_2O_3 are inserted individually at each temperature to highlight existing phases. Reflections of residual spinel structure in the 600 °C sample are marked with a star (*).

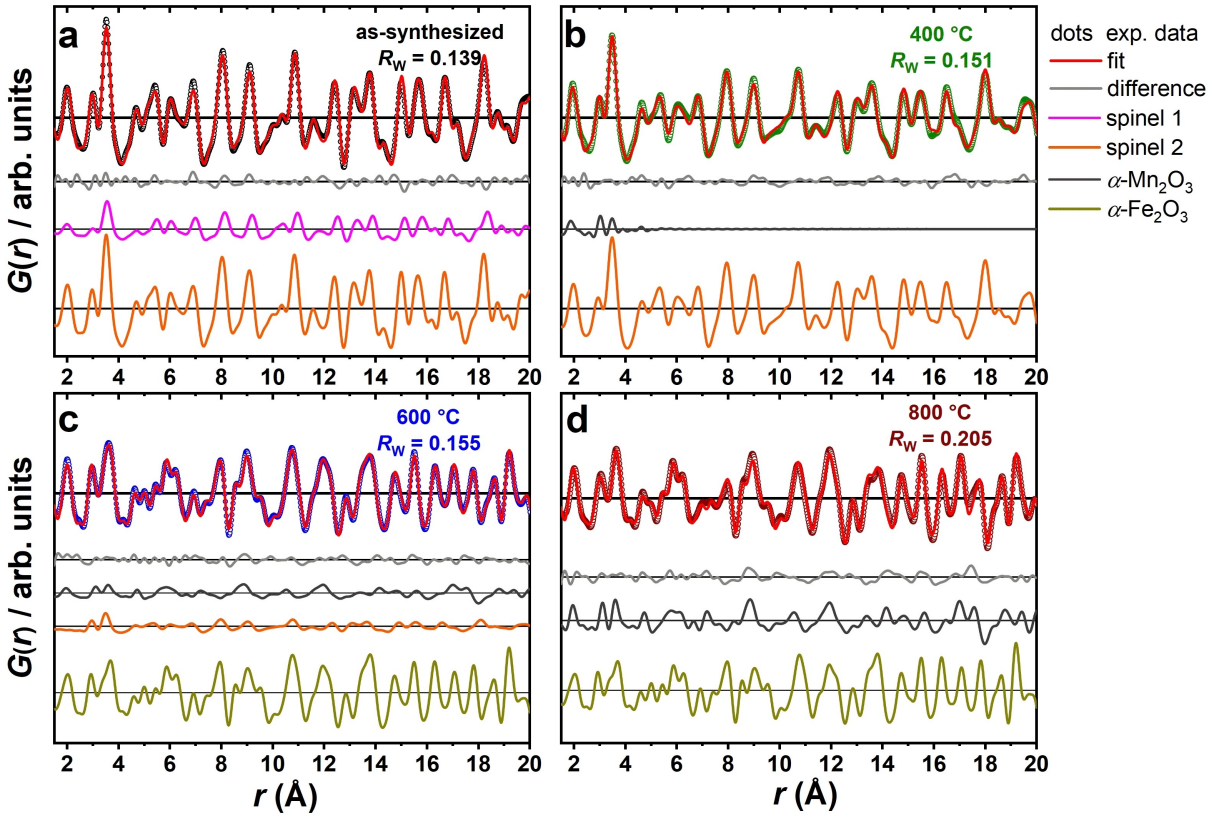

Figure 4. PDF refinements over 1.5 to 50 Å (shown range 1.5 to 20 Å) of the as-synthesized nanoparticles (a) and the ones after calcination at 400 (b), 600 (c), and 800 °C (d). Dots and red solid lines correspond to measured and simulated PDFs. Grey solid lines are the differences. Further solid lines represent the contribution of two different spinel phases, α-Mn_2O_3, and α-Fe_2O_3 to the refinements, respectively. All contributions and differences are plotted in offset, for clarity. The full range PDF refinements over 1.5 to 50 Å are presented in the SI.

accompanied by a manganese oxide phase due to the oxidation of the Mn(II) ions, which only becomes visible by this sophisticated analysis. The refined lattice parameter of 8.343 Å for the spinel phase in the 400 °C sample is even shorter than in bulk Fe_3O_4 (8.394 Å). Considering the resulting molar phase contents in the PDF fits and the Mn:Fe ratio from EDXS of 0.52 (XPS: 0.50), the average spinel sum formula results in $Mn_{0.43}Fe_{2.57}O_4$ (from XPS ratio: $Mn_{0.4}Fe_{2.6}O_4$; for calculation see **eq. S1**). After calcination at 600 °C, highly crystalline α-Fe_2O_3 has formed and the phase fraction of α-Mn_2O_3 increased, with a simultaneous decrease of residual spinel phase with a goodness-of-fit of 0.16. The existence of a α-Mn_2O_3 and a α-Fe_2O_3 phase at 600 °C is coincident with earlier studies on the phase transitions of pure iron and manganese oxide nanoparticles as well as manganese ferrite nanoparticles. They revealed that Mn_5O_8 transforms into α-Mn_2O_3 at 550 °C[64] and Fe_3O_4 transforms into α-Fe_2O_3 between 400 and 500 °C.[65] Evidence for the phase separation of $MnFe_2O_4$ nanoparticles into α-Fe_2O_3 and α-Mn_2O_3 by annealing at 550 °C is also given.[66] A refinement of only the short-range of 1–20 Å (Figure S5a) does not further improve the fit (R_W = 0.15), showing that short- and medium-range order are equivalent. The fit of the 800 °C sample results in a higher R_W (0.21) than for the 600 °C sample, although the phase transition has further progressed and the crystallinity and particle size of the hematite phase is expected to be higher given the sharper PXRD Bragg peaks (*cf.* Figure 3). Yet, the difference curve of the PDF fit features structural residuals for $r > 15$ Å. This is substantiated with a better goodness-of-fit R_W = 0.16 for the short-range order of 1–20 Å (Figure S5b). The reason for this could be found in possibly polydispersity of the α-Fe_2O_3 and α-Mn_2O_3 domains or crystal defects. During thermal treatment at 600 and 800 °C, the averaged Mn:Fe ratio measured by EDXS stays constant (600 °C: 0.52, 800 °C: 0.51). Since the nanoparticulate structure is lost at such high temperatures, XPS as surface-sensitive technique with low investigation depths (few nm) yields not reliable results concerning the bulk composition.

To conclude, the presented microwave synthesis yields crystalline monomodal $MnFe_2O_4$ nanoparticles with average diameters of 6 nm. However, PXRD and PDF analyses reveal a compositional or structural gradient within the material, which could for example explain varying lattice parameters from particle surface to core or the co-presence of Fe-rich and Fe-poor domains. A subsequent calcination triggers phase transformations. At 400 °C, a spinel-phase with a shortened lattice parameter (presumably magnetite, Fe_3O_4) can be identified as main phase, still forming nanoparticles. Further, small amounts of amorphous α-Mn_2O_3 can be detected, resulting in the Fe-

enrichment in the spinel phase. Even higher temperatures (600 and 800 °C) result in the complete decomposition of the spinel structure to the binary compounds α-Fe_2O_3 and α-Mn_2O_3, with some residual spinel at 600 °C.

The four Mn–Fe–O samples were additionally investigated by Raman spectroscopy (Figure 5a). Raman spectra were measured using a green laser (wavelength 532 nm), operated with a low power of 0.3 W to avoid sample fluorescence. The as-synthesized sample features a broad signal at 609 cm^{-1}, which can be assigned to the A_{1g} symmetry mode of spinel-type nanoparticulate $MnFe_2O_4$.[67] According to previous results, a spinel with a shortened lattice parameter is the main phase at a calcination temperature of 400 °C (presumably Fe_3O_4), causing a shift of the A_{1g} signal to higher wavenumbers (653 cm^{-1}).[68] At 600 °C, alongside the Fe_3O_4 spinel (647 cm^{-1}), the prominent Raman bands of α-Fe_2O_3 dominate,[69] while the α-Mn_2O_3 bands additionally appear at 800 °C.[70]

Additional investigations with DRIFT spectroscopy (Figure 5b) reveal that as-synthesized nanoparticles contain organic residues. The –C–H stretching vibration bands at 2967–2860 cm^{-1} clearly indicate the presence of residual acetylacetone on the particle surfaces.[71] Additionally, the prominent bands at 1561 and 1435 cm^{-1} are caused by carbonyl groups of precursor residues.[72,73] The presence of adsorbed water is indicated by –O–H stretching vibrations at 3396 cm^{-1} and the H–O–H bending mode at 1656 cm^{-1}.[74,75] The formation of Fe–O and Mn–O bonds is further confirmed by the bands at 741 and 489 cm^{-1}.[76] The removal of organics on the particle surface can be achieved by a subsequent thermal treatment at 400 °C or higher, but calcination at 600 and 800 °C results in the decomposition of the spinel-type structure.

To prove the presence of organics on the sample surface with a second technique, TG analysis was performed, coupled with mass spectrometry to measure H_2O and CO_2 gas evolution traces (Figure S7). A loss of surface adsorbed water can be observed between 40 and 150 °C. This is followed by the loss of detected organic residues between 200 and 275 °C, as indicated by the delayed signal in the CO_2 mass spectrometry diagram. At a calcination temperature of 400 °C, organic precursor residues are mostly removed, which is also confirmed by DRIFT spectroscopy.

An important feature of $MnFe_2O_4$ nanoparticles for application is their strong magnetism, because of the incorporation of magnetic $3d^5$ high-spin Mn(II) and Fe(III) ions in the partially inverse spinel-type crystal structure. To investigate the influence of particle morphologies and phase compositions on the magnetic properties, synthesized Mn–Fe–O samples were investigated with SQUID magnetometry. The zero field cooled-field cooled (ZFC-FC) magnetization plots measured at 100 Oe are presented in Figure 6a. For the as-synthesized and 400 °C-treated nanoparticles, a characteristic ZFC-FC curve for nanoparticulate soft magnetic materials can be observed.[77,78] Comparatively, the 600 and 800 °C samples exhibit significantly lower magnetic moments in the ZFC-FC curves, which can be correlated to the decomposition of the spinel-type crystal structure into binary compounds α-Mn_2O_3 and α-Fe_2O_3 (*cf.* Figure 3). Consequently, the loss of the spinel-based antiferromagnetic interactions results in an overall reduced magnetic moment. However, the 600 °C sample still contains residual amounts of a spinel-type phase, presumably Fe_3O_4, which would explain the higher magnetic moment, compared to the 800 °C sample.[79] The blocking temperatures (T_B) were estimated by d(ZFC-FC)/d(T) plots,[80] which are depicted in Figure 6b. The blocking temperature of as-synthesized 6 nm $MnFe_2O_4$ nanoparticles is 32 K, which agrees well with previous results reported by Masala *et al.*[81] For the 400 °C sample, the blocking temperature is in the same range (53 K). At even higher calcination temperature (600 °C), the maximum gets broader (81–96 K), which can be correlated to particle growth and an increasing magnetic anisotropy. No blocking temperature can be estimated for the 800 °C sample, which shows a rather small magnetic moment.

The antiferromagnetic exchange interactions between A and B site cations with a 1:2 ratio in Mn–Fe spinels result in ferrimagnetic properties, compared to non-spinel binary compounds α-Mn_2O_3 and α-Fe_2O_3, which are both antiferromagnets.

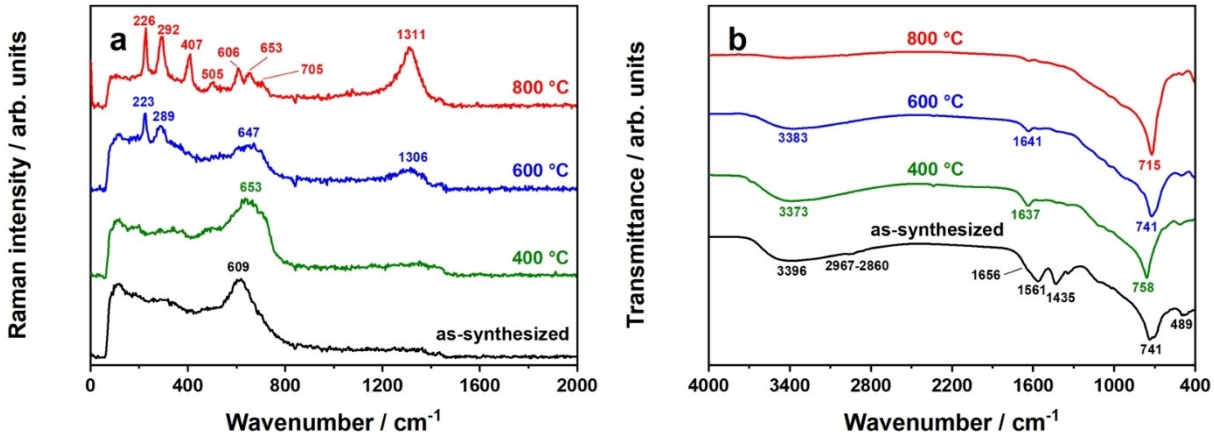

Figure 5. (a) Raman and (b) diffuse reflectance infrared Fourier transform (DRIFT) spectra of as-synthesized and calcined (400, 600, 800 °C) Mn–Fe–O samples. The spectra are stacked and scaled for clarity.

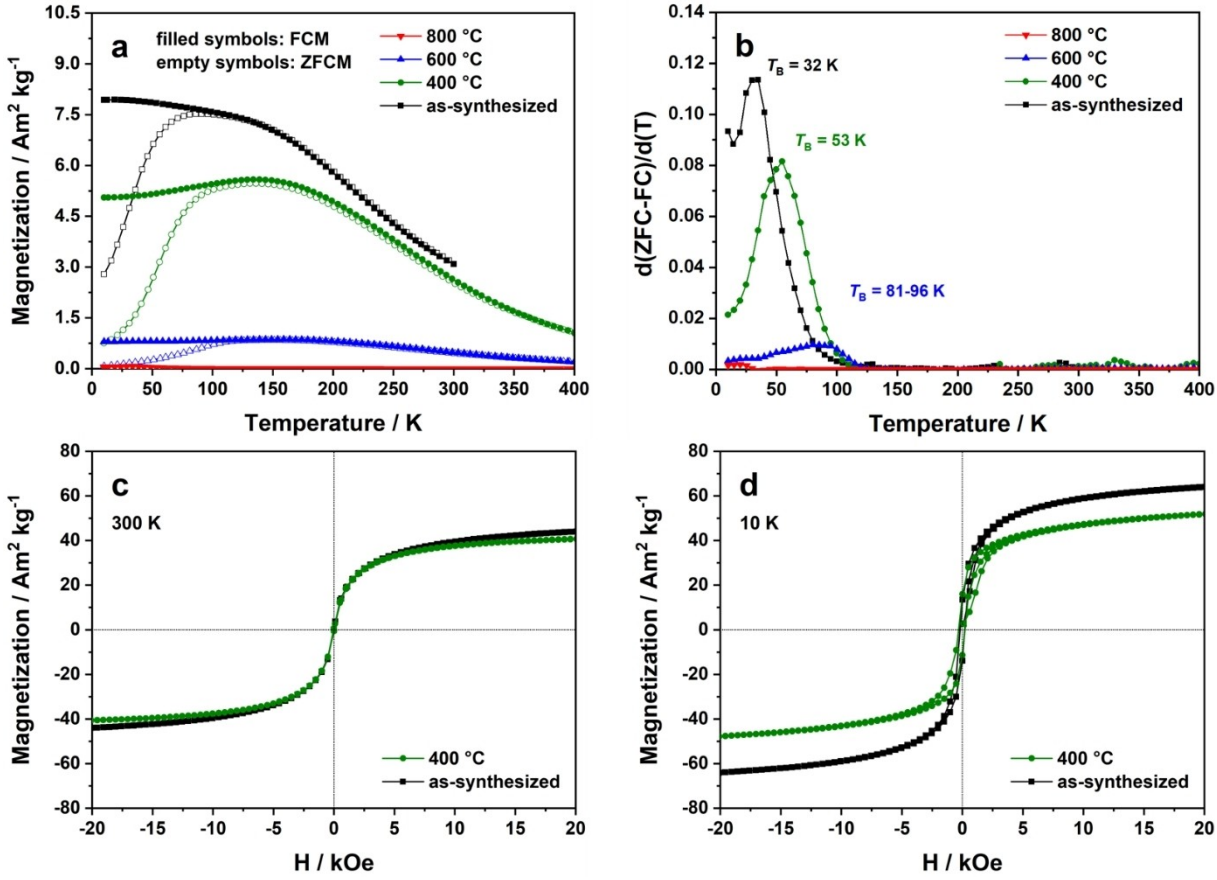

Figure 6. (a) Zero field cooled-field cooled (ZFC-FC) magnetization curves measured at 100 Oe and (b) d(ZFC-FC)/d(T) plots for as-synthesized and calcined (400, 600, 800 °C) Mn–Fe–O samples. Field scans were performed at 300 (c) and 10 K (d) for as-synthesized and 400 °C-treated samples and corrected with respect to the weight loss of diamagnetic components during calcination.

Thus, magnetization curves of as-synthesized and 400 °C nanoparticles were collected at 300 and 10 K (Figures 6c,d). For both samples, the magnetization curves were corrected with respect to the mass loss of diamagnetic carbon-containing residues (as-synthesized: 6.3 wt.-%, 400 °C: 1.3 wt.-%, *cf.* Figure S7). The uncorrected magnetization curves are additionally shown in Figures S8a,b. The saturation magnetizations (M_S) for both uncorrected and corrected data are summarized comparatively in Table 1. By applying the exponential LangevinMod fit,[63] corrected saturation magnetizations of as-synthesized $MnFe_2O_4$ nanoparticles could be estimated to 1.84 (300 K) and 2.62 μ_B (10 K) per formula unit (f.u.), respectively, which is equivalent to 44.5 (300 K) and 63.5 $Am^2 kg^{-1}$ (10 K). Thus, full saturation is not reached at 300 K. Compared to the maximum bulk value for $MnFe_2O_4$ of 3.3–4.5 μ_B,[21–23] the measured saturation magnetization for the 6 nm particles is significantly lower due to modified cationic distributions in the spinel structure and additional surface effects, like surface spin disorder.[82] In

Table 1. Saturation magnetizations of spinel nanoparticles, measured via SQUID magnetometry. The star (*) marks values, which were not corrected for the mass loss of diamagnetic carbon species. For the as-synthesized (as-syn) sample, a formula unit of $MnFe_2O_4$ ($M = 230.63\ g\,mol^{-1}$) and a unit cell of $Mn_8Fe_{16}O_{32}$ ($M = 1845.01\ g\,mol^{-1}$) were assumed. Due to progressing phase transitions to Fe_3O_4 at 400 °C, a formula unit of Fe_3O_4 ($M = 231.53\ g\,mol^{-1}$) and a unit cell of $Fe_{24}O_{32}$ ($M = 1852.24\ g\,mol^{-1}$) were presumed here.

		300 K			10 K		
	size/nm	M_S*/μ_B f.u.$^{-1}$	M_S/μ_B f.u.$^{-1}$	M_S/μ_B u.c.$^{-1}$	M_S*/μ_B f.u.$^{-1}$	M_S/μ_B f.u.$^{-1}$	M_S/μ_B u.c.$^{-1}$
as-syn	6.0	1.96	1.84	14.69	2.80	2.62	20.98
400 °C	6.3	1.73	1.71	13.68	2.07	2.05	16.36
	size/nm	M_S*/$Am^2 kg^{-1}$	M_S/$Am^2 g^{-1}$	M_S/$kAm^2 mol^{-1}$	M_S*/$Am^2 g^{-1}$	M_S/Am^2 g^{-1}	M_S/$kAm^2 mol^{-1}$
as-syn	6.0	47.5	44.5	82.1	67.8	63.5	117.2
400 °C	6.3	41.8	41.3	76.4	50.0	49.6	91.7

essence, prepared $MnFe_2O_4$ nanoparticles still reach higher saturation moments than other ferrites in the bulk state, *e.g.* $NiFe_2O_4$ or $MgFe_2O_4$.[24,27] The magnetic properties of $MnFe_2O_4$ can consequently be tailored for a particular application by preparing nanosized or bulk materials, which was already observed for other spinel-type materials.[17,83] The saturation magnetization decreases for 400 °C-treated nanoparticles to 1.71 (300 K) and 2.05 μ_B (10 K) per f.u., respectively, which corresponds to 41.3 (300 K) and 49.3 $Am^2 kg^{-1}$ (10 K). One possible explanation could be the transformation to a spinel structure with shortened lattice parameter, such as Fe_3O_4. However, magnetite nanoparticles were reported to reach similar saturation magnetizations like $MnFe_2O_4$.[29,84] But, nanoparticles treated at 400 °C already contain amorphous non-spinel α-Mn_2O_3 domains, which do not contribute to the overall magnetism and thus explain the reduced values satisfactorily. For both nanoparticulate samples, the magnetization curves measured at 10 K exhibit a hysteresis of 400–500 Oe, contrary to the ones collected at 300 K. Hence, synthesized particles are superparamagnetic at room temperature, as already indicated by the ZFC-FC magnetization plots.

In principle, correlations of magnetic properties and cationic distributions in Fe-based spinels can be investigated *via* ^{57}Fe Mössbauer spectroscopy. For this purpose, a magnetic hyperfine splitting in the Mössbauer spectrum is necessary.[8] However, this sextet splitting can only observed when the measurement temperature is lower than the respective blocking temperature (*e.g.* 32 K for the as-synthesized $MnFe_2O_4$ nanoparticles), which is why no inversion parameter could be estimated from the room temperature data (Figure S9). Due to superparamagnetism at room temperature, a broad doublet with a quadrupole splitting of ΔE_Q of 2.67 $mm\,s^{-1}$ was observed. The broadness with a FWHM = 1.94 $mm\,s^{-1}$ is based on the very small particle size of the sample. For the nanoparticles treated at 400 °C, the room temperature Mössbauer spectrum is even less defined and no fitting was possible. This is in line with the small particle size and the structural inhomogeneity of the spinel as observed by PXRD and PDF analysis.

Through the pronounced magnetism of microwave-derived manganese ferrite nanoparticles, they can be used as inorganic magnetic nanoparticles (MNPs) for numerous applications. Beyond this, the interesting properties of $MnFe_2O_4$ open further application fields. A special highlight is the use as visible-light responsive photocatalyst for hydrogen production or degradation reactions.[42–44] The optical properties of synthesized nanoparticles were therefore investigated by diffuse reflectance UV-Vis-NIR spectroscopy (Figure S10a). From the Kubelka Munk plot (Figure S10b),[85] the optical band gap energy of as-synthesized particles could be estimated to 1.6 eV (794 nm). Band gaps could be estimated more precisely by Tauc plots,[86] which are presented in Figures S10c,d for both direct and indirect behavior. Considering $MnFe_2O_4$ as indirect semiconductor,[87] Tauc analysis of as-synthesized $MnFe_2O_4$ nanoparticles reveals a band gap of 1.5 eV (821 nm). These findings highlight their ability to harvest sunlight. The estimated band gap value is in the same range with the literature value of 1.75–1.78 eV for $MnFe_2O_4$.[41] The progressing decompostion beginning at 400 °C to spinel Fe_3O_4 respective α-Mn_2O_3 and α-Fe_2O_3 effects a further shift of the band edge to the NIR range.

The use of $MnFe_2O_4$ nanoparticles for many applications, *e.g.* as ferrofluid or photocatalyst, requires a colloidal stabilization to achieve an improved dispersibilty in aqueous and non-aqueous media. Therefore, different stabilization strategies were applied. Since as-synthesized nanoparticles contain organic surface residues (*cf.* Figure 5b), postsynthetic stabilization with oleic acid/oleylamine (OA/OLA) seems reasonable to achieve dispersibilty in non-polar solvents, such as toluene.[48] Figure 7a shows the size distribution of OA/OLA-coated as-synthesized $MnFe_2O_4$ nanoparticles dispersed in toluene, measured *via* DLS. The size distribution is relatively sharp, with a mean hydrodynamic diameter of 33 nm, which shows that the particles are less agglomerated. The phase-transfer to polar media (*e.g.* water) was achieved by the exchange of the OA/OLA ligands with citric acid (Figure 7b).[49] The degree of agglomeration is significantly higher, which is reflected by the mean hydrodynamic diameter of 164 nm and the second signal at 500–1300 nm in the DLS measurement. Here, ligand stripping of $MnFe_2O_4$ nanoparticle surfaces with a Meerwein's salt could be helpful, prior to the coating with *e.g.* citric acid.[88] Another possibility of the stabilization of as-synthesized $MnFe_2O_4$ nanoparticles is the functionalization with betaine hydrochloride, which does however not improve the dispersibility in polar solvents (Figure 7c). Obviously, the organic residues on the nanoparticle surface hinder the betaine functionalization. To prove this suggestion, spinel nanoparticles calcined at 400 °C were also stabilized with betaine hydrochloride. Upon calcination at 400 °C, these organics are removed from the nanoparticle surface successfully, resulting in a more hydrophilic surface. Hence, the functionalization of calcined nanoparticles with betaine hydrochloride is possible, which is reflected by the corresponding DLS data (Figure 7d). The mean hydrodynamic diameter of 24 nm indicates a very low degree of agglomeration, and therefore a better dispersibilty.

Conclusion

Phase-pure $MnFe_2O_4$ nanoparticles were successfully synthesized *via* non-aqueous microwave-based sol-gel technique. Directly after synthesis, crystalline nanoparticles with 6 nm in diameter were obtained. Structural analysis reveals a spinel-type structure, with a lattice parameter near the literature value for $MnFe_2O_4$. The slight deviation could be explained with varying lattice parameters from particle surface to core or the co-presence of Fe-rich and Fe-poor domains. The as-synthesized $MnFe_2O_4$ nanoparticles are superparamagnetic at room temperature and ferrimagnetic at 10 K, reaching a saturation magnetization of 2.62 μ_B per formula unit (63.5 $Am^2 kg^{-1}$) at this temperature. Calcination at 400 °C effects no significant morphological changes. But, due to the early formation of amorphous α-Mn_2O_3, the spinel gets Fe richer. The lattice parameter shortens and fits better to Fe_3O_4, compared to $MnFe_2O_4$. The beginning phase decomposition diminishes the applicability of 400 °C-treated particles, which is, inter alia,

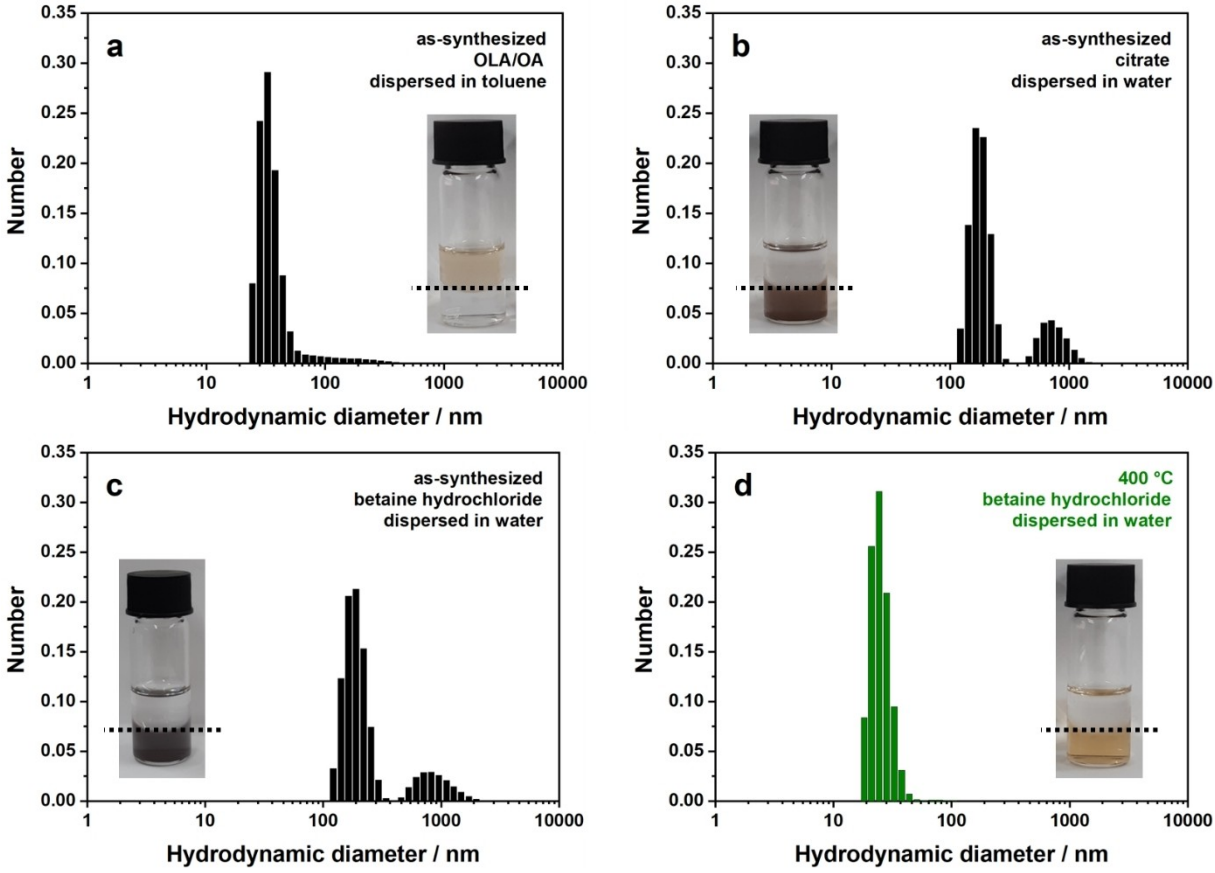

Figure 7. DLS measurements of as-synthesized $MnFe_2O_4$ nanoparticles, which were postsynthetically functionalized with oleic acid/oleylamine (OA/OLA) (a), citric acid (b), and betaine hydrochloride (c). The 400 °C-treated particles were also stabilized with betaine hydrochloride (d). Sample were dispersed in water (below) or toluene (above the broken line in insets), depending on the applied stabilization technique.

reflected by the reduced saturation magnetization of 2.05 μ_B (49.3 Am^2kg^{-1}). At even higher temperature of 600 or 800 °C, the spinel decomposes completely into binary non-spinel compounds α-Mn_2O_3 and α-Fe_2O_3, which is coupled with the loss of the typical magnetic properties of spinel ferrite compounds. We have demonstrated the possibility of the postsynthetic stabilization of magnetic 6 nm $MnFe_2O_4$ nanoparticles in polar and non-polar media, using citric acid respective oleic acid/oleylamine as stabilizing agents, which enables their use as *e.g.* ferrofluid or photocatalyst. The 400 °C-treated spinel nanoparticles, which exhibits a slightly changed composition, could also be stabilized in polar media by betaine hydrochloride.

Experimental section

Synthesis

For the synthesis of $MnFe_2O_4$ nanoparticles, a microwave-assisted synthesis of MFe_2O_4 spinel nanoparticles (M = Mg, Zn) published by Kirchberg *et al.* and Dolcet *et al.* was adapted.[50,59] Therefore, 126.6 mg (0.5 mmol) of $Mn(acac)_2$ (*Sigma Aldrich*, ≥ 97 %) and 353.2 mg (1.0 mmol) of $Fe(acac)_3$ (*Acros Organics*, > 99 %) were dissolved in 15 mL of *rac*-1-phenylethanol (*Sigma Aldrich*, 98 %) using ultrasonification. The obtained solution was transferred into a 30 mL borosilicate glass vessel and heated to 250 °C using a laboratory microwave reactor (*Anton Paar* Monowave 400 with MAS autosampler, frequency 2.45 GHz). The reaction temperature was kept for 30 minutes, before cooling to 55 °C with compressed air. During the microwave treatment, the solution was constantly stirred (600 rpm). The particles were subsequently precipitated with *n*-pentane, washed with acetone-water mixtures (3×) and diethyl ether. Finally, the nanoparticles were dried at 80 °C overnight. Optional thermal treatment of dried particles was performed in a muffle furnace under air atmosphere at 400, 600, and 800 °C for 1 h (heating rate: 10 $K min^{-1}$).

Postsynthetic colloidal stabilization

The stabilization tests were performed according to experimental protocols published by Kirchberg *et al.*[50] For postsynthetic stabilization of as-synthesized $MnFe_2O_4$ nanoparticles in non-polar solvents (*e.g.* toluene), 41.8 mg of $MnFe_2O_4$ were added to a solution of 2 mL of oleic acid (OA, *Sigma Aldrich*, 90 %), 2 mL of oleylamine (OLA, *Sigma Aldrich*, ≥ 98 %), and 20 mL of toluene (*VWR*, AnalaR Normapur®). The mixture was then refluxed at 116 °C for 48 hours. The nanoparticles were afterwards precipitated with methanol (*VWR*, AnalaR Normapur®) and dried at 80 °C. For the

phase-transfer into polar solvents (*e.g.* water), 25.6 mg of citric acid monohydrate (*Carl Roth*, ≥99.5%) were dissolved in 1.9 mL of 1,2-dichlorobenzene (*Alfa Aesar*, 99%) and 1.9 mL of *N*,*N*-dimethylformamide (*Alfa Aesar*, 99.8%). Then, 29.1 mg of the OA/OLA-coated $MnFe_2O_4$ nanoparticles were added to this solution. The mixture was heated to 100 °C for 22 hours. Finally, the citrate-stabilized particles were precipitated with diethyl ether, washed with acetone (3x), and dried at 80 °C.

As-synthesized $MnFe_2O_4$ nanoparticles were further stabilized in polar media using betaine hydrochloride. Therefore, 21.5 mg of $MnFe_2O_4$ were dissolved in 20 mL of a 2 wt.–% solution of betaine hydrochloride (*TCI*, >98%) in water. After stirring for 6 hours, particles were precipitated with acetone and dried at 80 °C. This procedure was additionally performed for the 400 °C-treated nanoparticles.

Characterization techniques

Transmission electron microscopy (TEM) and selected area electron diffraction (SAED) were performed on a 200 kV JEOL JEM-2200FS EFTEM from *JEOL GmbH*, additionally equipped with Schottky FEG and In-Column Omega Energyfilter. Prior to the measurements, approximately 1 mg of the sample were dispersed in ethanol (*Acros Organics*, extra dry, 99.5%), before dropping 4 µL of the dispersion on a carbon film-coated TEM grid (*ScienceServices*, 200 Mesh). Then, the sample was allowed to dry at room temperature. TEM images and SAED patterns were edited using ImageJ 1.52a.

For N_2 physisorption analysis at 77 K, an *Anton Paar* QUADRASORB evo surface area & pore size analyzer was used. Specific surface areas were estimated by applying the BET model (*Brunauer-Emmett-Teller*).[89] Samples were degassed in vacuum at 120 °C for 12 hours before the measurements. Data were evaluated with ASiQwin 4.0®.

Energy-dispersive X-ray spectroscopy (EDXS) was performed on a *Zeiss* Leo 1530 scanning electron microscope, combined with an UltraDry-EDX detector (*Thermo Fisher Scientific* NS7). Prior to the measurements, samples were sputtered with platinum with a Cressington Sputter Coater 208 HR. An acceleration voltage of 15 kV was applied during the measurements. The working distance was set to 8.0 mm.

X-ray photoelectron spectroscopy (XPS) was measured using a *Physical Electronics* PHI VersaProbe III Scanning XPS Microprobe equipped with a monochromatic aluminum K_α source. The survey scans were measured with a pass energy of 226 eV, a step size of 0.4 eV and a time of 50 ms per step, applying a beam diameter of 100 µm. All samples were flooded with low energy electrons and argon ions to prevent surface charging. The recorded data was evaluated with CasaXPS.

Ag powder X-ray diffraction (PXRD) data for PDF analysis was collected at room temperature on a *STOE* STADI P Mythen2 4 K diffractometer (Ag $K\alpha_1$, $\lambda = 0.5594$ Å).[90] Samples were measured in 0.5 mm diameter glass capillaries (*Hilgenberg* glass number 10) for 22 h each in a *Q*-range of 0.3 to 20.4 $Å^{-1}$. PDF processing was carried out with xPDFsuite[91] using a sample-dependent Q_{max} of 13.0 to 17.5 $Å^{-1}$, and fitting was done with PDFgui.[92] Refined parameters are the scale, lattice parameters, crystallite size, correlated atomic motion parameter λ_2, occupancy of octahedral sites in spinel structures and thermal parameters.

Cu PXRD (Cu $K\alpha_1$, $\lambda = 1.5405$ Å and Cu $K\alpha_2$, $\lambda = 1.5444$ Å) was performed on a *Malvern PANanalytical* Empyrean diffractometer with PixCel 1D detector. The device was operated at an acceleration voltage of 40 kV and an emission current of 40 mA. To reduce X-ray fluorescence, the pulse-height-discrimination (PHD) levels were changed to 8.05 and 11.27 keV, respectively. Data were recorded in a range of 10–70 2θ.

A *WITec* alpha 300 RA+ imaging system was employed for Raman measurements, equipped with a UHTS 300 spectrometer and a back-illuminated *Andor Newton* 970 EMCCD camera. The measurements were conducted at an excitation wavelength of $\lambda = 532$ nm, using a laser power of 0.3 mW, an integration time of 5 s and typically 20–30 accumulations (50x *Zeiss* objective, NA = 0.7, software *WITec* Control FIVE 5.3). All spectra were subjected to a cosmic ray removal routine and baseline correction.

For diffuse reflectance infrared Fourier transform (DRIFT) spectroscopy, a *Bruker* alpha II device was used. Data were collected with a spectral resolution of 10 cm^{-1} and 200 co-additions per scan.

Thermogravimetric (TG) analysis in synthetic air was performed using a *Netzsch* Jupiter STA 449 C thermo-balance, which was coupled with a *Netzsch* Aeolos QMS 403 C quadrupol mass spectrometer (MS) for detecting gaseous substances, such as H_2O (18) and CO_2 (44). The heating ramp was set to 10 K min^{-1}.

Magnetic measurements were performed on a superconducting quantum interference device (SQUID) MPMS-XL5 from *Quantum Design*. Prior to the measurements, samples were prepared in gelatin capsules, which were held by a plastic straw. The field measurements at 10 and 300 K were performed from 100 to 20000 to −20000 Oe (hysteresis mode), with a step width of 500 Oe. Data were corrected for the diamagnetism of the sample holder and the weight loss during thermal treatment. For estimation of the saturation magnetizations M_s, an exponential LangevinMod fit was applied, with the C parameter giving M_s. Saturation magnetizations were converted to units of μ_B per formula unit (f.u.) throughout the text. For recording zero field cooled-field cooled (ZFC-FC) magnetization data, samples were cooled in the SQUID cavity without applying an external magnetic field. The temperature scans were performed from 10 to 300/400 to 10 K in the sweep mode with a velocity of 5 K (applied field 100 Oe).

^{57}Fe Mössbauer spectroscopy was performed in a transmission geometry at constant acceleration with a conventional Mössbauer spectrometer with a ^{57}Co source (50 mCi), embedded in Rh. The spectra were fitted using *Recoil* 1.05 Mössbauer analysis software. The isomer shift values were corrected with respect to α-Fe as a reference at room temperature.

A *PerkinElmer* Lambda 750 device with Praying Mantis mirror unit was applied for diffuse reflectance (DR) UV-Vis-NIR measurements. Data were collected from 200 to 3000 nm, with a step size of 1 nm.

Dynamic light scattering (DLS) was used to determine the hydrodynamic diameter of the dispersed nanoparticles (0.5 mg mL^{-1}). After ultrasonic treatment, the dispersions were analysed in quartz cuvettes with a *Malvern* ZS Nano Zetasizer (20 °C, equilibration time 2 min, backscattering angle 173°). A refractive index of 2.39 was assumed for data evolution.[50] For each sample, three individual measurements were performed.

Acknowledgements

A.B. and R.M. gratefully acknowledge financial support from the AiF within the program for promoting the Industrial Collective Research (IGF) of the German Federal Ministry of Economic Affairs and Energy (BMWi), based on a resolution of the German Parliament (project "QuinoLight", 18904N1-5). C.S. and R.M. further acknowledge funding by the German Research Founda-

tion DFG (MA 5392/7-1). M.E. and M.Z. acknowledge funding by the DFG *via* SFB 840, project C7, and a scholarship of the Young Academy of the Bavarian Academy of Sciences and Humanities. H.K. gratefully acknowledges financial support from the MINT Lehramt Plus and the BayNAT program. The authors thank the Bavarian Polymer Institute KeyLab Electron and Optical Microscopy for the use of the EM setups. Further thanks go to Jonas Jungmann (University of Bayreuth, Department of Chemistry) for N_2 physisorption measurements, Michael Furtmair (University of Bayreuth, Department of Chemistry) for his help with DLS measurements, Dr. Holger Schmalz (University of Bayreuth, Keylab Synthesis and Molecular Characterization, Bavarian Polymer institute) for Raman-AFM analysis, and Lena Geiling (University of Bayreuth, Faculty of Engineering) for performing TG-MS experiments. We finally thank Bavarian Polymer Institute KeyLab Device Engineering and Dr. Morten Weiss (University of Bayreuth, Department of Chemistry) for the XPS measurements. Open Access funding enabled and organized by Projekt DEAL.

Conflict of Interest

The authors declare no conflict of interest.

Keywords: Spinel ferrites · magnetic nanoparticles · pair distribution function · colloidal stabilization · microwave synthesis

[1] V. F. Cardoso, A. Francesko, C. Ribeiro, M. Bañobre-López, P. Martins, S. Lanceros-Mendez, *Adv. Healthcare Mater.* **2018**, *7*, 1700845.
[2] Z. Zhou, L. Yang, J. Gao, X. Chen, *Adv. Mater.* **2019**, *31*, 1804567.
[3] S. Sun, *Science* **2000**, *287*, 1989–1992.
[4] C. Jiang, C. W. Leung, P. W. T. Pong, *Appl. Surf. Sci.* **2017**, *419*, 692–696.
[5] J. Govan, Y. Gun'ko, *Nanomaterials* **2014**, *4*, 222–241.
[6] F. Davodi, E. Mühlhausen, M. Tavakkoli, J. Sainio, H. Jiang, B. Gökce, G. Marzun, T. Kallio, *ACS Appl. Mater. Interfaces* **2018**, *10*, 31300–31311.
[7] D. Beketova, M. Motola, H. Sopha, J. Michalicka, V. Cicmancova, F. Dvorak, L. Hromadko, B. Frumarova, M. Stoica, J. M. Macak, *ACS Appl. Nano Mater.* **2020**, *3*, 1553–1563.
[8] C. Simon, J. Timm, D. Tetzlaff, J. Jungmann, U. Apfel, R. Marschall, *ChemElectroChem* **2021**, *8*, 227–239.
[9] R. Valenzuela, *Phys. Res. Int.* **2012**, *2012*, 1–9.
[10] L. B. Railsback, *Geology* **2003**, *31*, 737–740.
[11] Y. Goto, *Jpn. J. Appl. Phys.* **1964**, *3*, 309–313.
[12] J. M. Hastings, L. M. Corliss, *Rev. Mod. Phys.* **1953**, *25*, 114–119.
[13] M. L. Néel, *Ann. Phys. (Paris).* **1948**, *12*, 137–198.
[14] D. S. Mathew, R.-S. Juang, *Chem. Eng. J.* **2007**, *129*, 51–65.
[15] J.-R. Huang, C. Cheng, *J. Appl. Phys.* **2013**, *113*, 33912.
[16] Y. Wang, L. Li, Y. Zhang, X. Chen, S. Fang, G. Li, *J. Phys. Chem. C* **2017**, *121*, 19467–19477.
[17] A. Bloesser, H. Kurz, J. Timm, F. Wittkamp, C. Simon, S. Hayama, B. Weber, U.-P. Apfel, R. Marschall, *ACS Appl. Nano Mater.* **2020**, *3*, 11587–11599.
[18] S. M. Ansari, B. B. Sinha, D. Phase, D. Sen, P. U. Sastry, Y. D. Kolekar, C. V. Ramana, *ACS Appl. Nano Mater.* **2019**, *2*, 1828–1843.
[19] K. Vamvakidis, M. Katsikini, D. Sakellari, E. C. Paloura, O. Kalogirou, C. Dendrinou-Samara, *Dalton Trans.* **2014**, *43*, 12754–12765.
[20] M. J. Thompson, K. J. Blakeney, S. D. Cady, M. D. Reichert, J. Del Pilar-Albaladejo, S. T. White, J. Vela, *Chem. Mater.* **2016**, *28*, 1668–1677.
[21] G. Balaji, N. Gajbhiye, G. Wilde, J. Weissmüller, *J. Magn. Magn. Mater.* **2002**, *242–245*, 617–620.
[22] M. Zheng, X. Wu, B. Zou, Y. Wang, *J. Magn. Magn. Mater.* **1998**, *183*, 152–156.
[23] Z. X. Tang, C. M. Sorensen, K. J. Klabunde, G. C. Hadjipanayis, *Phys. Rev. Lett.* **1991**, *67*, 3602–3605.
[24] A. Berkowitz, J. Lahut, C. VanBuren, *IEEE Trans. Magn.* **1980**, *16*, 184–190.
[25] A. Ceylan, S. Ozcan, C. Ni, S. Ismat Shah, *J. Magn. Magn. Mater.* **2008**, *320*, 857–863.
[26] M. Y. Rafique, M. Ellahi, M. Z. Iqbal, Q. Javed, L. Pan, *Mater. Lett.* **2016**, *162*, 269–272.
[27] V. Šepelák, I. Bergmann, D. Menzel, A. Feldhoff, P. Heitjans, F. J. Litterst, K. D. Becker, *J. Magn. Magn. Mater.* **2007**, *316*, e764–e767.
[28] S. Maensiri, M. Sangmanee, A. Wiengmoon, *Nanoscale Res. Lett.* **2009**, *4*, 221–228.
[29] G. F. Goya, T. S. Berquó, F. C. Fonseca, M. P. Morales, *J. Appl. Phys.* **2003**, *94*, 3520–3528.
[30] O. Schneeweiss, R. Zboril, N. Pizurova, M. Mashlan, E. Petrovsky, J. Tucek, *Nanotechnology* **2006**, *17*, 607–616.
[31] D. H. Han, J. P. Wang, H. L. Luo, *J. Magn. Magn. Mater.* **1994**, *136*, 176–182.
[32] R. Pauthenet, *Ann. Phys. (Paris).* **1952**, *12*, 710–747.
[33] M. Gonzalez-Sandoval, A. Beesley, M. Miki-Yoshida, L. Fuentes-Cobas, J. Matutes-Aquino, *J. Alloys Compd.* **2004**, *369*, 190–194.
[34] Z. Simsa, V. Brabers, *IEEE Trans. Magn.* **1975**, *11*, 1303–1305.
[35] F. Nesa, A. K. M. Zakaria, M. A. S. Khan, S. M. Yunus, A. K. Das, S.-G. Eriksson, M. N. I. Khan, M. A. Hakim, *World J. Condens. Matter Phys.* **2012**, *2*, 27–35.
[36] H. Štěpánková, B. Sedlák, V. Chlan, P. Novák, Z. Šimša, *Phys. Rev. B* **2008**, *77*, 92416.
[37] J. M. Hastings, L. M. Corliss, *Phys. Rev.* **1956**, *104*, 328–331.
[38] U. König, *Solid State Commun.* **1971**, *9*, 425–427.
[39] Z. J. Zhang, Z. L. Wang, B. C. Chakoumakos, J. S. Yin, *J. Am. Chem. Soc.* **1998**, *120*, 1800–1804.
[40] J. P. Chen, C. M. Sorensen, K. J. Klabunde, G. C. Hadjipanayis, E. Devlin, A. Kostikas, *Phys. Rev. B* **1996**, *54*, 9288–9296.
[41] A. Mary Jacintha, A. Manikandan, K. Chinnaraj, S. Arul Antony, P. Neeraja, *J. Nanosci. Nanotechnol.* **2015**, *15*, 9732–9740.
[42] K. Dhanalaxmi, R. Yadav, S. K. Kundu, B. M. Reddy, V. Amoli, A. K. Sinha, J. Mondal, *Chem. A Eur. J.* **2016**, *22*, 15639–15644.
[43] M. Pal, R. Rakshit, K. Mandal, *ACS Appl. Mater. Interfaces* **2014**, *6*, 4903–4910.
[44] H. B. Desai, L. J. Hathiya, H. H. Joshi, A. R. Tanna, *Mater. Today: Proc.* **2020**, *21*, 1905–1910.
[45] S. R. Patade, D. D. Andhare, S. B. Somvanshi, S. A. Jadhav, M. V. Khedkar, K. M. Jadhav, *Ceram. Int.* **2020**, *46*, 25576–25583.
[46] X. Wu, Y. Niu, B. Feng, Y. Yu, X. Huang, C. Zhong, W. Hu, C. M. Li, *ACS Appl. Mater. Interfaces* **2018**, *10*, 20440–20447.
[47] R. E. Hewitt, H. F. Chappell, J. J. Powell, *Curr. Opin. Toxicol.* **2020**, *19*, 93–98.
[48] R. M. Patil, P. B. Shete, N. D. Thorat, S. V. Otari, K. C. Barick, A. Prasad, R. S. Ningthoujam, B. M. Tiwale, S. H. Pawar, *RSC Adv.* **2014**, *4*, 4515–4522.
[49] M. Lattuada, T. A. Hatton, *Langmuir* **2007**, *23*, 2158–2168.
[50] K. Kirchberg, A. Becker, A. Bloesser, T. Weller, J. Timm, C. Suchomski, R. Marschall, *J. Phys. Chem. C* **2017**, *121*, 27126–27138.

[51] B. Aslibeiki, P. Kameli, H. Salamati, M. Eshraghi, T. Tahmasebi, *J. Magn. Magn. Mater.* **2010**, *322*, 2929–2934.
[52] Y. Wang, R. Cheng, Z. Wen, L. Zhao, *Eur. J. Inorg. Chem.* **2011**, *2011*, 2942–2947.
[53] M. M. Cruz, L. P. Ferreira, J. Ramos, S. G. Mendo, A. F. Alves, M. Godinho, M. D. Carvalho, *J. Alloys Compd.* **2017**, *703*, 370–380.
[54] J. Azadmanjiri, H. K. Salehani, *Phys. Status Solidi* **2007**, *4*, 253–255.
[55] I. Bilecka, M. Niederberger, *Nanoscale* **2010**, *2*, 1358.
[56] V. Šepelák, U. Steinike, D. C. Uecker, S. Wißmann, K. D. Becker, *J. Solid State Chem.* **1998**, *135*, 52–58.
[57] R. Deshmukh, M. Niederberger, *Chem. A Eur. J.* **2017**, *23*, 8542–8570.
[58] L. Zhang, G. Garnweitner, I. Djerdj, M. Antonietti, M. Niederberger, *Chem. Asian J.* **2008**, *3*, 746–752.
[59] P. Dolcet, K. Kirchberg, A. Antonello, C. Suchomski, R. Marschall, S. Diodati, R. Muñoz-Espí, K. Landfester, S. Gross, *Inorg. Chem. Front.* **2019**, *6*, 1527–1534.
[60] C. Simon, M. B. Zakaria, H. Kurz, D. Tetzlaff, A. Blösser, M. Weiss, J. Timm, B. Weber, U. Apfel, R. Marschall, *Chem. A Eur. J.* **2021**, doi.org/10.1002/chem.202101716.
[61] L. Passerini, *Gazz. Chim. Ital.* **1930**, *60*, 389–99.
[62] J. I. Langford, A. J. C. Wilson, *J. Appl. Crystallogr.* **1978**, *11*, 102–113.
[63] M. Eckardt, S. L. J. Thomä, M. Dulle, G. Hörner, B. Weber, S. Förster, M. Zobel, *ChemistryOpen* **2020**, *9*, 1214–1220.
[64] S. R. Cooper, R. O. Candler, A. G. Cosby, D. W. Johnson, K. M. Ø. Jensen, J. E. Hutchison, *ACS Nano* **2020**, *14*, 5480–5490.
[65] U. Topal, M. A. Aksan, *J. Magn. Magn. Mater.* **2016**, *406*, 123–128.
[66] F. Al-Mokdad, R. S. Hassan, R. Awad, *Curr. Nanomater.* **2019**, *4*, 125–136.
[67] W. Wang, Z. Ding, X. Zhao, S. Wu, F. Li, M. Yue, J. P. Liu, *J. Appl. Phys.* **2015**, *117*, 17A328.
[68] N. H. Hai, N. D. Phu, N. H. Luong, N. Chau, H. D. Chinh, L. H. Hoang, D. L. Leslie-Pelecky, *J. Korean Phys. Soc.* **2008**, *52*, 1327–1331.
[69] D. L. A. de Faria, S. Venâncio Silva, M. T. de Oliveira, *J. Raman Spectrosc.* **1997**, *28*, 873–878.
[70] R. Naeem, M. Ali Ehsan, R. Yahya, M. Sohail, H. Khaledi, M. Mazhar, *Dalton Trans.* **2016**, *45*, 14928–14939.
[71] S. F. Tayyari, T. Bakhshi, S. J. Mahdizadeh, S. Mehrani, R. E. Sammelson, *J. Mol. Struct.* **2009**, *938*, 76–81.
[72] B. Eckhardt, E. Ortel, D. Bernsmeier, J. Polte, P. Strasser, U. Vainio, F. Emmerling, R. Kraehnert, *Chem. Mater.* **2013**, *25*, 2749–2758.
[73] C. R. Vestal, Z. J. Zhang, *J. Am. Chem. Soc.* **2003**, *125*, 9828–9833.
[74] A. M. Turek, I. E. Wachs, E. DeCanio, *J. Phys. Chem.* **1992**, *96*, 5000–5007.
[75] N. Gajbhiye, G. Balaji, *Thermochim. Acta* **2002**, *385*, 143–151.
[76] Q. Chen, J. Zheng, Q. Yang, Z. Dang, L. Zhang, *ACS Appl. Mater. Interfaces* **2019**, *11*, 15478–15488.
[77] P. A. Joy, P. S. Anil Kumar, S. K. Date, *J. Phys. Condens. Matter* **1998**, *10*, 11049–11054.
[78] C. Liu, B. Zou, A. J. Rondinone, Z. J. Zhang, *J. Phys. Chem. B* **2000**, *104*, 1141–1145.
[79] M. Ahmadzadeh, C. Romero, J. McCloy, *AIP Adv.* **2018**, *8*, 56807.
[80] K. L. Livesey, S. Ruta, N. R. Anderson, D. Baldomir, R. W. Chantrell, D. Serantes, *Sci. Rep.* **2018**, *8*, 11166.
[81] O. Masala, R. Seshadri, *Chem. Phys. Lett.* **2005**, *402*, 160–164.
[82] R. H. Kodama, A. E. Berkowitz, E. J. McNiff, S. Foner, *J. Appl. Phys.* **1997**, *81*, 5552–5557.
[83] D. K. Dinkar, B. Das, R. Gopalan, B. S. Dehiya, *Mater. Chem. Phys.* **2018**, *218*, 70–76.
[84] Y. Wei, B. Han, X. Hu, Y. Lin, X. Wang, X. Deng, *Procedia Eng.* **2012**, *27*, 632–637.
[85] P. Kubelka, F. Munk, *Z. Tech. Phys.* **1931**, *12*, 593–601.
[86] J. Tauc, *Mater. Res. Bull.* **1968**, *3*, 37–46.
[87] A. R. O. Rodrigues, J. M. F. Ramos, I. T. Gomes, B. G. Almeida, J. P. Araújo, M. J. R. P. Queiroz, P. J. G. Coutinho, E. M. S. Castanheira, *RSC Adv.* **2016**, *6*, 17302–17313.
[88] A. Dong, X. Ye, J. Chen, Y. Kang, T. Gordon, J. M. Kikkawa, C. B. Murray, *J. Am. Chem. Soc.* **2011**, *133*, 998–1006.
[89] S. Brunauer, P. H. Emmett, E. Teller, *J. Am. Chem. Soc.* **1938**, *60*, 309–319.
[90] S. L. J. Thomae, N. Prinz, T. Hartmann, M. Teck, S. Correll, M. Zobel, *Rev. Sci. Instrum.* **2019**, *90*, 43905.
[91] X. Yang, P. Juhas, C. L. Farrow, S. J. L. Billinge, *J. Appl. Crystallogr.* **2014**, arXiv:1402.3163v3.
[92] C. L. Farrow, P. Juhas, J. W. Liu, D. Bryndin, E. S. Božin, J. Bloch, T. Proffen, S. J. L. Billinge, *J. Phys. Condens. Matter* **2007**, *19*, 335219.

Manuscript received: May 31, 2021
Revised manuscript received: August 30, 2021
Accepted manuscript online: September 3, 2021

